JCI The Journal of Clinical Investigation

Heparan sulfate deficiency disrupts developmental angiogenesis and causes congenital diaphragmatic hernia

Bing Zhang, … , Jeffrey D. Esko, Lianchun Wang

J Clin Invest. 2014;124(1):209-221. https://doi.org/10.1172/JCI71090.

Research Article **Vascular biology**

Congenital diaphragmatic hernia (CDH) is a common birth malformation with a heterogeneous etiology. In this study, we report that ablation of the heparan sulfate biosynthetic enzyme NDST1 in murine endothelium (*Ndst1*^{ECKO} mice) disrupted vascular development in the diaphragm, which led to hypoxia as well as subsequent diaphragm hypoplasia and CDH. Intriguingly, the phenotypes displayed in *Ndst1*^{ECKO} mice resembled the developmental defects observed in slit homolog 3 (*Slit3*) knockout mice. Furthermore, introduction of a heterozygous mutation in roundabout homolog 4 (*Robo4*), the gene encoding the cognate receptor of SLIT3, aggravated the defect in vascular development in the diaphragm and CDH. NDST1 deficiency diminished SLIT3, but not ROBO4, binding to endothelial heparan sulfate and attenuated EC migration and in vivo neovascularization normally elicited by SLIT3-ROBO4 signaling. Together, these data suggest that heparan sulfate presentation of SLIT3 to ROBO4 facilitates initiation of this signaling cascade. Thus, our results demonstrate that loss of NDST1 causes defective diaphragm vascular development and CDH and that heparan sulfate facilitates angiogenic SLIT3-ROBO4 signaling during vascular development.

Find the latest version:

https://jci.me/71090/pdf

Heparan sulfate deficiency disrupts developmental angiogenesis and causes congenital diaphragmatic hernia

Bing Zhang,[1] Wenyuan Xiao,[1] Hong Qiu,[1] Fuming Zhang,[2] Heather A. Moniz,[1] Alexander Jaworski,[3] Eduard Condac,[1] Gerardo Gutierrez-Sanchez,[1] Christian Heiss,[1] Robin D. Clugston,[4] Parastoo Azadi,[1] John J. Greer,[4] Carl Bergmann,[1] Kelley W. Moremen,[1] Dean Li,[5] Robert J. Linhardt,[2] Jeffrey D. Esko,[6] and Lianchun Wang[1]

[1]Department of Biochemistry and Molecular Biology and Complex Carbohydrate Research Center, University of Georgia, Athens, Georgia, USA. [2]Department of Chemistry and Chemical Biology, Department of Chemical and Biological Engineering, Center for Biotechnology and Interdisciplinary Studies, Rensselaer Polytechnic Institute, Troy, New York, USA. [3]Department of Neuroscience, Brown University, Providence, Rhode Island, USA. [4]Department of Physiology, Centre for Neuroscience, Women and Children's Health Research Institute, University of Alberta, Edmonton, Alberta, Canada. [5]Molecular Medicine Program, University of Utah, Salt Lake City, Utah, USA. [6]Department of Cellular and Molecular Medicine, Glycobiology Research and Training Center, University of California at San Diego, La Jolla, California, USA.

Congenital diaphragmatic hernia (CDH) is a common birth malformation with a heterogeneous etiology. In this study, we report that ablation of the heparan sulfate biosynthetic enzyme NDST1 in murine endothelium (*Ndst1*^{ECKO} mice) disrupted vascular development in the diaphragm, which led to hypoxia as well as subsequent diaphragm hypoplasia and CDH. Intriguingly, the phenotypes displayed in *Ndst1*^{ECKO} mice resembled the developmental defects observed in slit homolog 3 (*Slit3*) knockout mice. Furthermore, introduction of a heterozygous mutation in roundabout homolog 4 (*Robo4*), the gene encoding the cognate receptor of SLIT3, aggravated the defect in vascular development in the diaphragm and CDH. NDST1 deficiency diminished SLIT3, but not ROBO4, binding to endothelial heparan sulfate and attenuated EC migration and in vivo neovascularization normally elicited by SLIT3-ROBO4 signaling. Together, these data suggest that heparan sulfate presentation of SLIT3 to ROBO4 facilitates initiation of this signaling cascade. Thus, our results demonstrate that loss of NDST1 causes defective diaphragm vascular development and CDH and that heparan sulfate facilitates angiogenic SLIT3-ROBO4 signaling during vascular development.

Introduction

Congenital diaphragmatic hernia (CDH), a common malformation affecting 1 in 3,000 live births, has been associated with significant perinatal mortality (1). The hallmark of CDH is rupture of the diaphragm and herniation of the liver, gut, and intestine into the thoracic cavity. Based on its anatomical location, CDH is classified into Bochdalek, Morgagni, and central tendon hernias (1, 2). Bochdalek hernia is most common and occurs through the Bochdalek canal or foramen in the posterior diaphragm. Morgagni and central tendon hernias result from defects in anterior and central tendon, respectively. Diaphragmatic hernias can occur in isolation, but in many cases, they affect lung development and cardiac function (2). The etiology of CDH appears to be heterogeneous. To date, 48 gene mutations, deletions, and/or duplications have been associated with CDH, including mutations in genes encoding transcriptional factors such as Fog2, GATA4, WT1, COUPTFII, and MyoD and extracellular signaling components including FGFR, PDGFR, MMPs, glypican-3 (GPC3), roundabout 1 (ROBO1), and slit homolog 3 (SLIT3) (3, 4).

Examination of patient specimens and animal models attribute CDH to a developmental abnormality of diaphragmatic mesenchymal tissue and tendon (4, 5). The diaphragm consists of skeletal muscle, underlying mesenchyme, connective tissues (tendon), phrenic nerve, and blood vessels. Skeletal muscle originates during development from the paraxial mesoderm (5). The central tendon is derived from transverse septum, a part of the splanchnic mesoderm. The phrenic nerve branches from the central nervous system and innervates the developing diaphragm. Blood vessels in the diaphragm consist of arteries, veins, and capillaries, forming a well-defined network that supplies nutrients and oxygen to the diaphragm. These originate from the descending aorta, inferior vena cava, and vasculature of the chest wall. It is unknown whether this vascular developmental defect contributes to CDH.

Heparan sulfate (HS) is a linear polysaccharide composed of glucosamine and uronic acid residues (glucuronic acid or iduronic acid) arranged in disaccharide repeats that are sulfated to a variable extent. In tissues, HS is covalently attached to core proteins of a small set of proteoglycans (HSPGs) that include glypicans, syndecans, perlecan, collagen XVIII, and agrin (6). HS chains can interact with various growth factors, growth factor receptors, and extracellular matrix proteins to regulate cell proliferation, apoptosis, adhesion, and migration. Intriguingly, the loss-of-function mutation of *GPC3* was reported to cause Simpson-Golabi-Behmel syndrome, including the clinical spectrum of CDH (7). However, the molecular and cellular mechanism underling CDH due to *GPC3* deficiency was not determined. In the present study, we found that EC-specific inactivation of *N*-deacetylase-*N*-sulfotransferase-1 (*Ndst1*), a gene that initiates modification reactions during HS biosynthesis, caused highly penetrant central-type CDH in mice due to disruption of diaphragmatic vascular development mediated by HS-SLIT3-ROBO4 signaling. Our results dem-

Conflict of interest: The authors have declared that no conflict of interest exists.
Citation for this article: *J Clin Invest.* 2014;124(1):209–221. doi:10.1172/JCI71090.

onstrated that defects in diaphragmatic developmental angiogenesis can contribute to CDH, revealed *NDST1* as a candidate gene that might explain cases of CDH of unknown etiology, and showed that HS essentially facilitated angiogenic SLIT3-ROBO4 signaling during development.

Results

Mice deficient in endothelial Ndst1 develop postnatal CDH. *Ndst1–Ndst4* encode dual-function enzymes that initiate the processing of HS by *N*-deacetylation and *N*-sulfation of a subgroup of *N*-acetylglucosamine residues. Mouse ECs express high levels of *Ndst1* and *Ndst2* transcripts, a low amount of *Ndst3*, and no *Ndst4* (8). We selectively ablated *Ndst1* expression in ECs by breeding *Ndst1*$^{f/f}$ mice, which contain a conditionally targeted allele of *Ndst1* (*Ndst1*^{f}), with transgenic *Tie2Cre* mice, generating *Tie2Cre*$^{+}$*Ndst1*$^{f/f}$ (referred to herein as *Ndst1*^{ECKO}) mice (8, 9). Deficiency of NDST1 in mouse ECs resulted in a 50%–60% reduction of *N*-, 2-*O*–, and 6-*O*–sulfation in HS, showing that NDST1 plays a dominant role in endothelial HS modification (8, 9). *Ndst1*^{ECKO} mice thrived and reproduced normally; however, 40% developed CDH at P2, with penetrance rising to 60% (72 of 120) in adults (Figure 1, A and B). CDH occurred at the anterior midline of the septum transversum in the diaphragm (Figure 1A), reminiscent of central-type CDH in humans. In most affected animals, the liver was the only herniated organ, but in a few cases, the small intestine was involved (Figure 1A). Hernia size did not progress with age, and the penetrance and severity of the phenotype did not differ between male and female mice. *Ndst1*^{ECKO} mice developed normal pulmonary structure (Supplemental Figure 1A; supplemental material available online with this article; doi:10.1172/JCI71090DS1) and did not show signs of lung dysfunction that occurs in severe CDH. In summary, endothelial *Ndst1* deficiency caused isolated, central-type CDH without affecting other major organs.

Loss of endothelial Ndst1 disturbs diaphragm development prior to CDH onset. CDH is a developmental abnormality, which suggests that *Ndst1*^{ECKO} mice might exhibit a hypoplastic diaphragm. To address this issue, we initially examined diaphragms at P1, the day prior to CDH onset. Histological examination showed that the diaphragm covering the liver was thinner than that of littermate *Ndst1*$^{f/f}$ controls (Figure 1C). Masson's trichrome staining revealed that the covering connective tissue mainly consisted of collagen fibers embedded with mesothelial cells, indicative of tendon tissue. In the central diaphragmatic tendon in *Ndst1*$^{f/f}$ mice, collagen fibers were abundant and well organized and contained well-differentiated, spindle-shaped tenocytes. In contrast, the collagen bundle in *Ndst1*^{ECKO} diaphragm was poorly expressed and disorganized, with fewer tenocytes (Figure 1C). Since the collagen bundle is the major carrier for tendon force, dysgenesis of the collagen bundles may represent the underlying explanation for tendon rupture and herniation in *Ndst1*^{ECKO} diaphragm after birth. We suspect that herniation occurs after birth as a result of added stress imposed by stomach expansion and intestine distension from feeding.

The central tendon and the liver were completely separated in *Ndst1*$^{f/f}$ mice, but remained fused together in *Ndst1*^{ECKO} animals at P1 (Figure 1C), which suggests that *Ndst1*^{ECKO} diaphragm development was delayed during embryogenesis. Examination of the primordial tendon at E15.5 confirmed that the genesis of the central tendon in *Ndst1*^{ECKO} diaphragm was similarly disrupted, showing decreased thickness and disorganized fibrils compared with the *Ndst1*$^{f/f}$ control (Figure 1, D and E). H&E staining showed that the muscular region of the *Ndst1*^{ECKO} diaphragm was also thinner than in *Ndst1*$^{f/f}$ mice (Figure 1F). However, fasciculi in *Ndst1*^{ECKO} diaphragm muscle were well organized, and the ultrastructure of the sarcomere (Z- and M-band and myofibril) was well aligned and expressed (Supplemental Figure 1B). Phrenic nerve dysgenesis was previously reported to contribute to CDH pathogenesis (5). However, phrenic neural innervation in *Ndst1*^{ECKO} diaphragm appeared normal, with no change in gross axonal patterning (i.e., number of primary and secondary branches, motor axon fasciculation, and innervation of neuromuscular junctions; Supplemental Figure 1, C and D). Collectively, these findings suggest that diaphragm dysgenesis occurs mainly in the central tendon region and prior to CDH onset in *Ndst1*^{ECKO} mice.

Loss of endothelial Ndst1 leads to vascularization defects in the developing diaphragm. *Tie2Cre*-mediated gene ablation has been previously shown to be panendothelial (10). Examination of *Tie2Cre*$^{+}$*Rosa26LacZ* mice showed that LacZ expression in E15.5 diaphragm was restricted to the phrenic artery and vein, the intercostal artery and capillaries in the muscular compartment, and the central tendon (Figure 2A), which indicates that *Ndst1* most likely underwent recombination as well. Immnuofluorescence staining of the diaphragmatic tendon and muscle with the monoclonal antibody 10E4, which binds to *N*-sulfated domains in HS, showed staining that colocalized with the EC marker PECAM-1. 10E4 staining was lost in *Ndst1*^{ECKO} diaphragmatic ECs (Figure 2B), which indicates that NDST1 inactivation diminished *N*-sulfation of diaphragmatic endothelial HS. HS expression in other diaphragm tissues, including muscle, ligament, and nerve, was not altered. Therefore, *Tie2Cre*-mediated NDST1 recombination occurred efficiently in the endothelium of developing diaphragm.

To determine whether *Ndst1* inactivation affected developmental angiogenesis, E15.5–E16.5 diaphragms were whole-mount stained for PECAM-1 (Figure 2C). At E15.5, *Ndst1*$^{f/f}$ central tendon was well vascularized, except for a small dorsal region; the avascular region in *Ndst1*^{ECKO} central tendon was much larger. At E16.5, full vascularization had occurred in *Ndst1*$^{f/f}$ mice, whereas formation of the capillary bed in the same region in *Ndst1*^{ECKO} mice remained incomplete (Figure 2C). In addition, *Ndst1*^{ECKO} vasculature in tendon exhibited reduced vessel density and many missing connections. Quantification of capillary branch point number and vessel length confirmed the significant reduction of vascular density in *Ndst1*^{ECKO} tendon (Figure 2D). The primary plexus of blood vessels in *Ndst1*^{ECKO} diaphragmatic muscle had normal arteriovenous branching and patterning at E14.5 and E15.5 (Figure 2E). However, close observation with confocal 3D scanning microscopy demonstrated fewer vascular floors and reduced vascular density in *Ndst1*^{ECKO} versus *Ndst1*$^{f/f}$ mice: some *Ndst1*^{ECKO} capillaries were slender and cord-like (Figure 2E), suggestive of poor lumenization. At E18.5, *Ndst1*^{ECKO} capillary density remained reduced (Figure 2F). Adult animals showed reduced branches of large vessels in the anterior muscular region of septum transversum (Figure 2G and Supplemental Figure 2A). Interestingly, tissue sections of major organs, including brain, liver, kidney, heart, lung, spleen, and thymus, did not exhibit any obvious alteration of capillary density or structure in *Ndst1*^{ECKO} mice (Supplemental Figure 2B).

Loss of NDST1 impairs endothelial motility and proliferation, but not mural cell coverage. To determine whether *Ndst1* inactivation affected tip ECs, which guide angiogenic sprouting, we examined whole-mount–stained central tendon for PECAM-1. On average, 3 tip cells per counting field were observed in *Ndst1*$^{f/f}$ mice, compared with

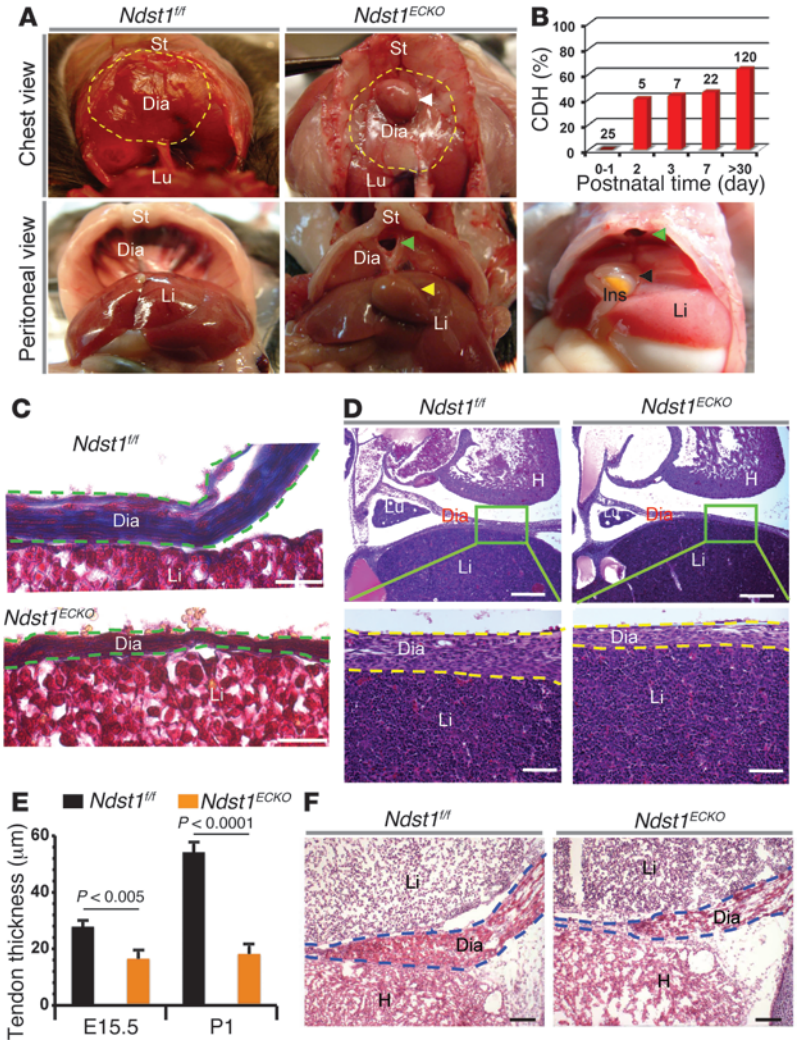

Figure 1

Ndst1^{ECKO} mice develop CDH due to central tendon dysgenesis. (**A**) Anatomical portrait of CDH in *Ndst1*^{ECKO} mice. Dashed yellow outline, anterior region of diaphragm (Dia); white arrowhead, hernia; green arrowhead, sac at the central tendon region; yellow arrowhead, herniated liver (Li); black arrowhead, herniated intestine (Ins); St, sternum; Lu, lung. (**B**) Onset and penetrance of CDH in *Ndst1*^{ECKO} mice. Hernias began to occur as early as P2, with penetrance rising to 46% at P7 and 60% in adult mice. *n* is shown above each bar. (**C**) Collagen staining. P1 tissue sections were stained for collagen with Masson's trichrome. Diaphragm (dashed green outline) showed substantially reduced collagen fiber (blue) expression in *Ndst1*^{ECKO} mice. (**D**) H&E staining of E15.5 central tendon. Dashed yellow outline, diaphragm. (**E**) Thickness of diaphragm central tendon regions. *Ndst1*^{ECKO} central tendon thickness was significantly reduced compared with *Ndst1*$^{f/f}$ littermate controls at both E15.5 and P1 ($n = 4$). (**F**) H&E staining of E18.5 diaphragm. *Ndst1*^{ECKO} diaphragm showed reduced thickness and attenuated muscle integrity. H, heart. Scale bars: 100 μm (**C**); 200 μm (**D**, top); 50 μm (**D**, bottom); 250 μm (**F**).

1 tip cell in *Ndst1*^{ECKO} animals (Figure 3A). Furthermore, the filopodia of *Ndst1*^{ECKO} tip cells were fewer in number and much shorter. *Ndst1*^{ECKO} EC proliferation was also reduced, as measured by BrdU incorporation: approximately 11.5% of ECs in *Ndst1*$^{f/f}$ tendon were BrdU^{+}, compared with approximately 7% of *Ndst1*^{ECKO} tendon ECs (Figure 3B). Thus, *Ndst1* ablation resulted in a loss of tip cells, disrupted filopodia, and reduced EC proliferation, contributing to overall vascular dysgenesis in the *Ndst1*^{ECKO} diaphragm.

The last step of angiogenesis is mural cell (MC) recruitment, which is required to form mature vasculature. HS has been shown to be required in a cell-autonomous manner for MC recruitment and vascular maturation (11, 12). However, MCs spread and attached closely to *Ndst1*^{ECKO} endothelium and showed overall coverage comparable to that observed in *Ndst1*$^{f/f}$ endothelium, as measured by NG2 whole-mount staining (Figure 3C). Smooth muscle thickness in the larger arterioles was also normal. Therefore, endothelial *Ndst1* deficiency did not affect MC recruitment.

Defective vascular development leads to hypoxia and subsequent decrease in diaphragmatic cell survival and proliferation. Defective angiogenesis may result in ischemia, which leads to hypoxia of neighboring tissue. To test whether disrupted vascular development leads to hypoxia in *Ndst1*^{ECKO} diaphragm, pregnant mice were injected with a hypoxia indicator, Hypoxyprobe-1, which forms a protein adduct in tissue under low oxygen concentration. Examination of central tendon regions showed that approximately 23% of *Ndst1*^{ECKO} tenoblast cells stained positive for Hypoxyprobe-1, compared with 5% of *Ndst1*$^{f/f}$ cells (Figure 3D), illustrating a substantial increase of hypoxia in *Ndst1*^{ECKO} tendon. Severe hypoxia interrupts mitochondrial respiration and causes mitochondrial leakage and apoptosis (13). Apoptosis was increased in *Ndst1*^{ECKO} versus *Ndst1*$^{f/f}$ tendon (*Ndst1*^{ECKO}, 0.33%; *Ndst1*$^{f/f}$, 0.13%; Figure 3E). Hypoxia also reduced cell proliferation of *Ndst1*^{ECKO} tenocytes (Figure 3F). The finding of increased apoptosis with attenuated proliferation strongly suggests that *Ndst1*^{ECKO} diaphragm hypoplasia arises from hypoxia caused by defective vascular development.

The CDH phenotype of Ndst1^{ECKO} *mice is not attributable to defects in VEGF signaling.* To gain insight into the molecular mechanism underlying the angiogenic defect in *Ndst1*^{ECKO} mice, we initially speculated that endothelial *Ndst1* deficiency might disrupt VEGF signaling, based on our previous findings that endothelial *Ndst1* deletion attenuates VEGF signaling in tumor angiogenesis (9, 14). However, examination of VEGFR2 phosphorylation found no significant difference between *Ndst1*^{ECKO} and *Ndst1*$^{f/f}$ diaphragm at E18.5 (Figure 4A). Meanwhile, compounding heterozygous

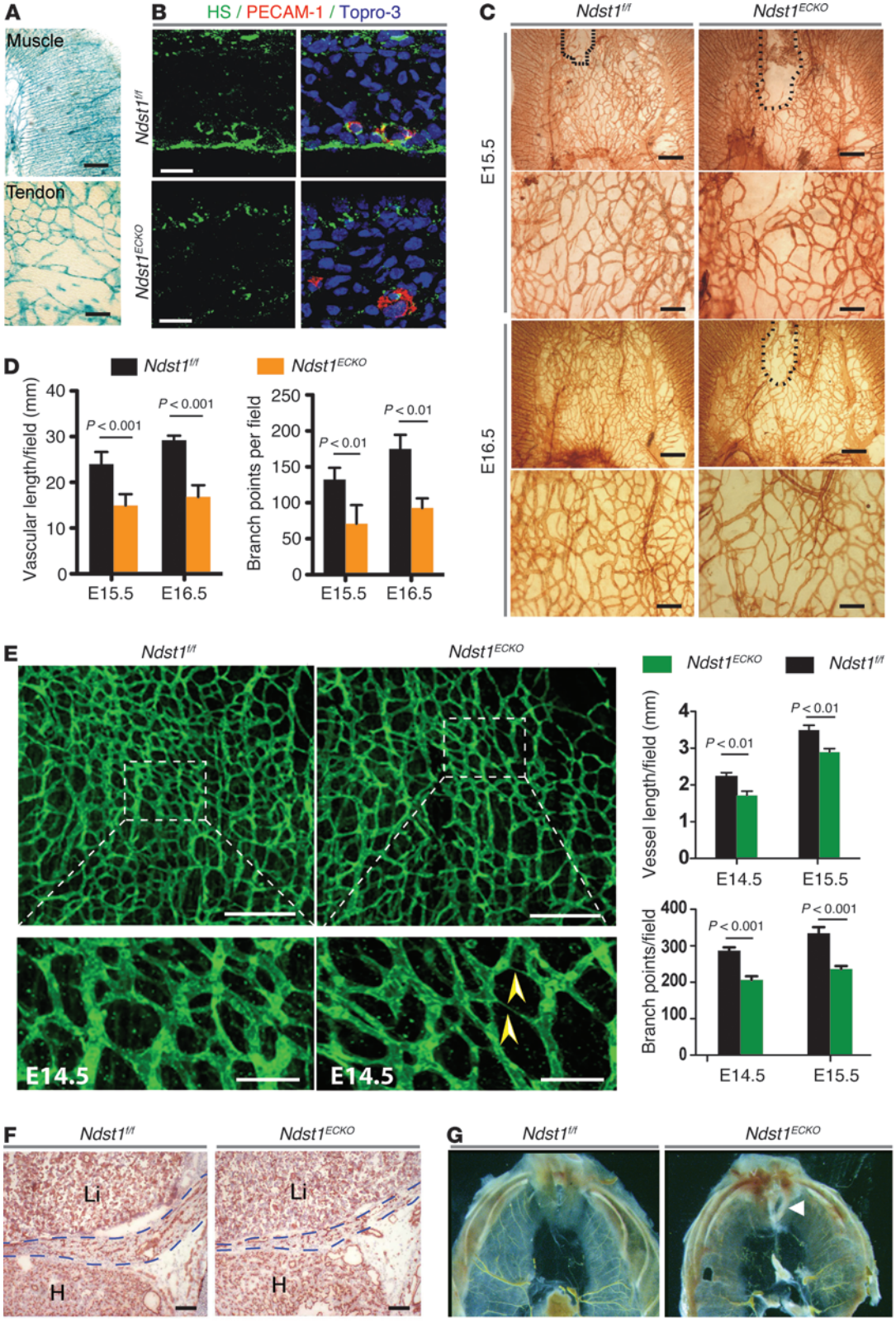
A
Muscle
Tendon
B
HS / PECAM-1 / Topro-3
Ndst1f/f
Ndst1ECKO
C
Ndst1f/f
Ndst1ECKO
E15.5
E16.5
D
Ndst1f/f
Ndst1ECKO
Vascular length/field (mm)
P < 0.001
P < 0.001
E15.5
E16.5
Branch points per field
P < 0.01
P < 0.01
E15.5
E16.5
E
Ndst1f/f
Ndst1ECKO
E14.5
E14.5
Ndst1ECKO
Ndst1f/f
Vessel length/field (mm)
P < 0.01
P < 0.01
E14.5
E15.5
Branch points/field
P < 0.001
P < 0.001
E14.5
E15.5
F
Ndst1f/f
Ndst1ECKO
Li
H
Li
H
G
Ndst1f/f
Ndst1ECKO

Figure 2
Ndst1^{ECKO} mice display disrupted vascularization in diaphragm. (**A**) Whole-mount X-gal staining of E15.5 *Tie2Cre^{+}Rosa26LacZ* diaphragm. The vascular plexus in diaphragm muscle and tendon was LacZ positive. (**B**) Costaining with anti-HS and anti–PECAM-1 antibodies showed that HS expressed by ECs was dramatically reduced in E15.5 *Ndst1^{ECKO}* diaphragm. Cell nuclei were stained with Topro-3. (**C**) Whole-mount staining of E15.5–E16.5 diaphragm with anti–PECAM-1 antibody. Vascular density in *Ndst1^{ECKO}* tendon was substantially reduced, with a larger avascular region (dotted outline). (**D**) Vascular length and branch point were both significantly decreased in E15.5–E16.5 *Ndst1^{ECKO}* tendons (n = 5–7 per time point). (**E**) Whole-mount staining of E14.5–E15.5 diaphragm with anti–PECAM-1 antibody. Vascular density was significantly reduced in the *Ndst1^{ECKO}* muscular region. Arrowheads, cord-like vessels. (**F**) Anti–PECAM-1 staining of E18.5 embryo showed reduced vascular density in *Ndst1^{ECKO}* diaphragm (dashed outlines). (**G**) Microfill gel perfusion highlighted vasculature in adult diaphragm. The vasculature of *Ndst1^{ECKO}* diaphragm lacked large vessels and was less branched in the anterior muscular region (see also Supplemental Figure 2A). Arrowhead, hernia sac. Scale bars: 0.5 mm (**A** and **C**, top); 10 μm (**B**); 0.2 mm (**C**, bottom; and **E**, top); 50 μm (**E**, bottom); 250 μm (**F**).

VEGFR2 (*VEGFR2$^{+/-}$*) mice, which are viable and also do not develop CDH (15), with *Ndst1^{ECKO}* did not alter CDH penetrance (Supplemental Figure 2C). The unaltered VEGFR2 phosphorylation and lack of a synergistic effect of *VEGFR2$^{+/-}$* with *Ndst1^{ECKO}* both indicate that the localized angiogenesis defect and subsequent CDH phenotype in *Ndst1^{ECKO}* mice is unlikely to be caused by disrupted VEGF/VEGFR2 signaling.

Central-type CDH in Ndst1^{ECKO} mice resembles developmental defects in Slit3$^{-/-}$ mice. A clue to the molecular mechanism underlying the angiogenic defect exhibited in *Ndst1^{ECKO}* mice emerged from our studies of *Slit3$^{-/-}$* mice, which displayed a similar phenotype (Figure 4B). We previously showed that SLIT3, although recognized as an axon guidance molecule, functions to promote EC proliferation and motility in vitro and angiogenesis in vivo (16). Immunostaining revealed abundant SLIT3 expression in diaphragmatic muscle and vasculature (Figure 4C). Staining of E15.5–E16.5 diaphragms for PECAM-1 showed that vascularization in *Slit3$^{-/-}$* tendon was largely impaired, especially in the anterior tendon regions (Figure 4D). *Slit3$^{-/-}$* tendon vessels also showed diverse diameters, and sprout discontinuity and vascular plexus density were dramatically reduced (Figure 4D and Supplemental Figure 3). Vascular density and sprouting in diaphragmatic muscle was similarly reduced (Figure 4E). Confocal images showed that microvessels in the diaphragm were conspicuously dilated and disorganized (Figure 4F). Rather than sprouting and communicating with neighboring vessels, some *Slit3$^{-/-}$* vessels terminated with large, distended heads with fewer extending filopodia (Figure 4F). Tip cells were also reduced by 89% in *Slit3$^{-/-}$* diaphragms (Figure 4G). Collectively, these observations illustrated that loss of SLIT3 results in vascular developmental defects similar to those seen in *Ndst1^{ECKO}* mice.

We attempted to demonstrate genetic interactions between *Ndst1* and *Slit3* by crossing *Ndst1^{ECKO}* and *Slit3$^{+/-}$* mice. However, we observed no difference in CDH penetrance between *Ndst1^{ECKO}Slit3$^{+/-}$* and *Ndst1^{ECKO}Slit3$^{+/+}$* mice (n = 341; Figure 4H), possibly due to insufficient reduction of SLIT3 expression in heterozygous mice (Supplemental Figure 4A). In contrast, 100% of *Ndst1^{ECKO}Slit3$^{-/-}$* mice developed CDH, compared with 57% of *Ndst1^{ECKO}* and 86% of *Slit3$^{-/-}$* mice, which suggests that interactions between these genes might exist. However, power analysis indicated that >500 *Ndst1^{ECKO}Slit3$^{-/-}$* and *Slit3$^{-/-}$* mice would be needed to determine statistical significance, making further genetic experiments of this nature impractical.

Robo4 genetically interacts with endothelial Ndst1. High expression of ROBO4, the cognate receptor for SLITs, has been reported in the vasculature during major organ development in mice (17, 18). *Robo4$^{+/-}$* mice bearing a *Robo4* allele marked by insertion of alkaline phosphatase (AP; ref. 18) exhibited staining for AP activity in the blood vessels in diaphragm, lung, liver, and other major organs in E13.3 mice (Figure 5A). Analysis of E15.5 whole-mounts showed that ROBO4 was abundantly expressed in all blood vessels in *Robo4$^{+/-}$* diaphragm (Figure 5B). These observations are consistent with previous reports (17, 19, 20) and support ROBO4 as a panvascular marker.

Clinical studies have noted an association of CDH in humans with a duplication of the distal region of chromosome 11q, which includes the *ROBO4* gene (21). We previously showed that SLIT3 binds ROBO4 to promote angiogenesis in vitro (16). We therefore speculated that endothelial NDST1 might modulate SLIT3 signaling through the ROBO4 pathway. To test this hypothesis, *Ndst1^{ECKO}* mice were bred with *Robo4$^{+/-}$* mice, and their offspring were examined (Figure 5C). E15.5 *Robo4$^{+/-}$* mice showed normal vascular development in the central tendon region. However, compounding of *Robo4$^{+/-}$* with *Ndst1^{ECKO}* delayed diaphragm vascularization and resulted in more severe vascular branching defects, including missing connections, lack of sprouting, and formation of coiled ends. E15.5 *Robo4$^{-/-}$* diaphragms showed slightly disrupted vascular development in the diaphragm, and compounding of *Robo4$^{-/-}$* with *Ndst1^{ECKO}* aggravated the angiogenic defects, as evidenced by a large avascular region in the anterior tendon and reduced total vessel length and branch point numbers compared with *Ndst1$^{f/f}$* control (*Ndst1^{ECKO}Robo4$^{+/-}$*, 57% and 63% reduction, respectively; *Ndst1^{ECKO}Robo4$^{-/-}$*, 76% and 78%; *Ndst1^{ECKO}Robo4$^{+/+}$*, 43% and 47%; $P < 0.01$; Figure 5D). The compound mutants also showed a dramatic increase in CDH penetrance that inversely correlated with *Robo4* gene dosage (*Ndst1^{ECKO}Robo4$^{+/+}$*, 48%; *Ndst1^{ECKO}Robo4$^{+/-}$*, 88%; *Ndst1^{ECKO}Robo4$^{-/-}$*, 92%; $P < 0.0001$; Figure 5E). These observations demonstrated a genetic interaction between *Robo4* and endothelial *Ndst1* during diaphragmatic vascular development and also suggested that a defect in HS-SLIT3-ROBO4 signaling represents the leading molecular mechanism underlying the CDH etiology in *Ndst1^{ECKO}* mice.

Loss of endothelial Ndst1 attenuates Slit3-induced angiogenesis. To directly examine whether endothelial NDST1 modulates angiogenesis elicited by SLIT3-ROBO4 in vivo, we carried out cornea micropocket angiogenesis experiments. In agreement with previous reports, FGF2 and SLIT3 both potently induced neovascularization in wild-type mice (16). In contrast, SLIT3-induced angiogenesis was greatly diminished in both *Robo4$^{-/-}$* and *Ndst1^{ECKO}* mice (Figure 6A and Supplemental Figure 4B). These observations showed that ROBO4 is the major receptor responsible for angiogenic induction by SLIT3 and requires HS for activity.

We also derived a mouse diaphragmatic EC line by large T antigen immortalization of primary diaphragmatic ECs from *Ndst1$^{f/f}$* mice. A *Ndst1$^{-/-}$* daughter cell line was then created by infecting the *Ndst1$^{f/f}$* cells with adeno-Cre followed by cell cloning. Structural analysis of HS isolated from the cells showed that *Ndst1* ablation reduced *N*- and 2-*O*–sulfation by 60% and

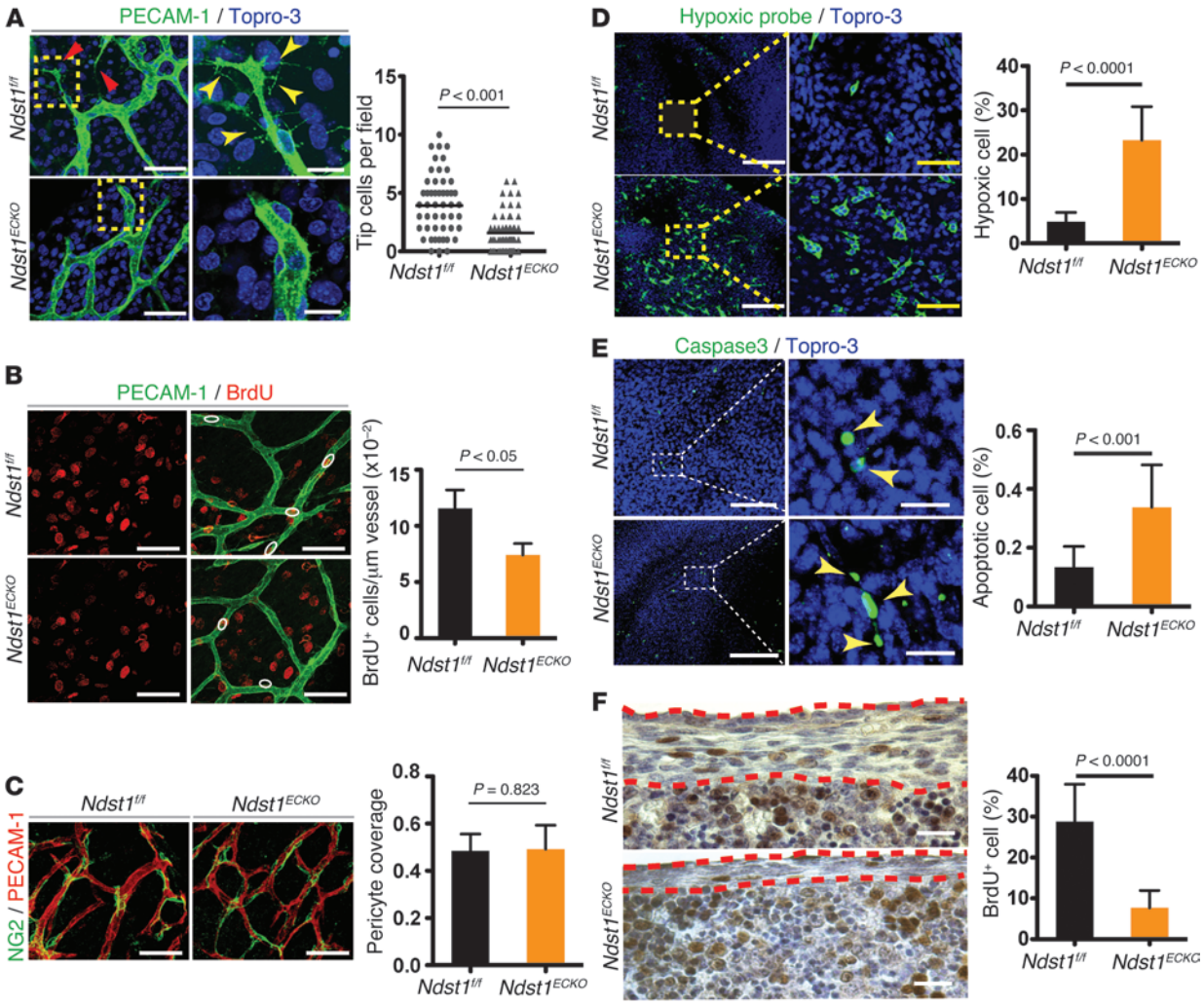

Figure 3

Hypoxia, increased apoptosis, and attenuated proliferation of tendon cells in developing *Ndst1*^{ECKO} diaphragm. (**A**) Vascular tip cells. Whole-mount costaining with anti–PECAM-1 antibody and Topro-3 showed tip cells (red arrows) and their characteristic structure as well as filopodia (yellow arrowheads), both of which were reduced in *Ndst1*^{ECKO} diaphragms at E16.5 (n = 6). (**B**) EC proliferation. Diaphragms from BrdU-injected E16.5 embryos were costained for BrdU and PECAM-1. BrdU$^+$ ECs (white outlines) were reduced in *Ndst1*^{ECKO} diaphragms (n = 5). (**C**) Pericyte recruitment. E16.5 diaphragms were immunostained with anti–PECAM-1 and anti-NG2 antibodies. Pericyte coverage did not differ in the *Ndst1*^{ECKO} and *Ndst1*$^{f/f}$ vasculature (n = 4–6). (**D**) Hypoxic tendon cells. E15.5 diaphragms were costained with anti-pimonidazole antibody and Topro-3 to visualize hypoxic cells. Hypoxic cells were much more prevalent in *Ndst1*^{ECKO} than in *Ndst1*$^{f/f}$ diaphragm tendon (n = 5). (**E**) Apoptotic tendon cells. E15.5 diaphragms were costained with anti–caspase-3 and Topro-3 to visualize apoptotic cells. Apoptotic endocytes (yellow arrowheads) were more prevalent in *Ndst1*^{ECKO} than in *Ndst1*$^{f/f}$ diaphragm (n = 4). (**F**) Proliferating tendon cells. Diaphragms from BrdU-injected E15.5 embryos were immunostained with anti-BrdU antibody. Red dashed outline, diaphragmatic tendon. BrdU$^+$ tendon cells were significantly reduced in *Ndst1*^{ECKO} diaphragms (n = 6). Scale bars: 40 μm (**A**, left; **B**; **C**; **D**, right; and **E**, right); 10 μm (**A**, right); 200 μm (**D**, left); 100 μm (**E**, left); 50 μm (**F**).

6-*O*–sulfation by 20% (Figure 6B and refs. 8, 9). Whereas *Ndst1*$^{f/f}$ ECs showed high cell surface SLIT3 binding, this was reduced in heparinase-treated *Ndst1*$^{f/f}$ cells and *Ndst1*$^{-/-}$ ECs (Figure 6C). In situ SLIT3 binding to diaphragmatic vessels was also attenuated (Figure 6D). In transwell assays, SLIT3 induced robust migration of *Ndst1*$^{f/f}$ cells, but not *Ndst1*$^{-/-}$ or heparinase-treated *Ndst1*$^{f/f}$ cells (Figure 6E). We also examined lung ECs derived from mice lacking *Ndst2*, the other major NDST isozyme expressed in ECs. *Ndst1*$^{f/f}$*Ndst2*$^{-/-}$ ECs express normal HS, whereas *Ndst1*$^{-/-}$*Ndst2*$^{-/-}$ (*Ndst1/2*$^{-/-}$) ECs express nonsulfated HS (8, 22). *Ndst1*$^{f/f}$*Ndst2*$^{-/-}$ ECs, but not *Ndst1/2*$^{-/-}$ cells, responded strongly to SLIT3-induced cell migration (Supplemental Figure 4C). Analysis of intracellular signaling showed that SLIT3 activated the Rho GTPase family members RhoA and Cdc42 in *Ndst1*$^{f/f}$*Ndst2*$^{-/-}$ ECs, but not in *Ndst1/2*$^{-/-}$ ECs (Supplemental Figure 4, D and E). Taken together, these observations demonstrated that EC HS functions in a cell-autonomous manner to facilitate SLIT3-ROBO4 signaling.

SLIT2 and ROBO1 have previously been shown to bind HS (23–26), which suggests that SLIT3 and ROBO4 might function in a similar manner to interact with endothelial HS. To test this idea, we generated the N-terminal fragments of SLIT3 (SLIT3-N)

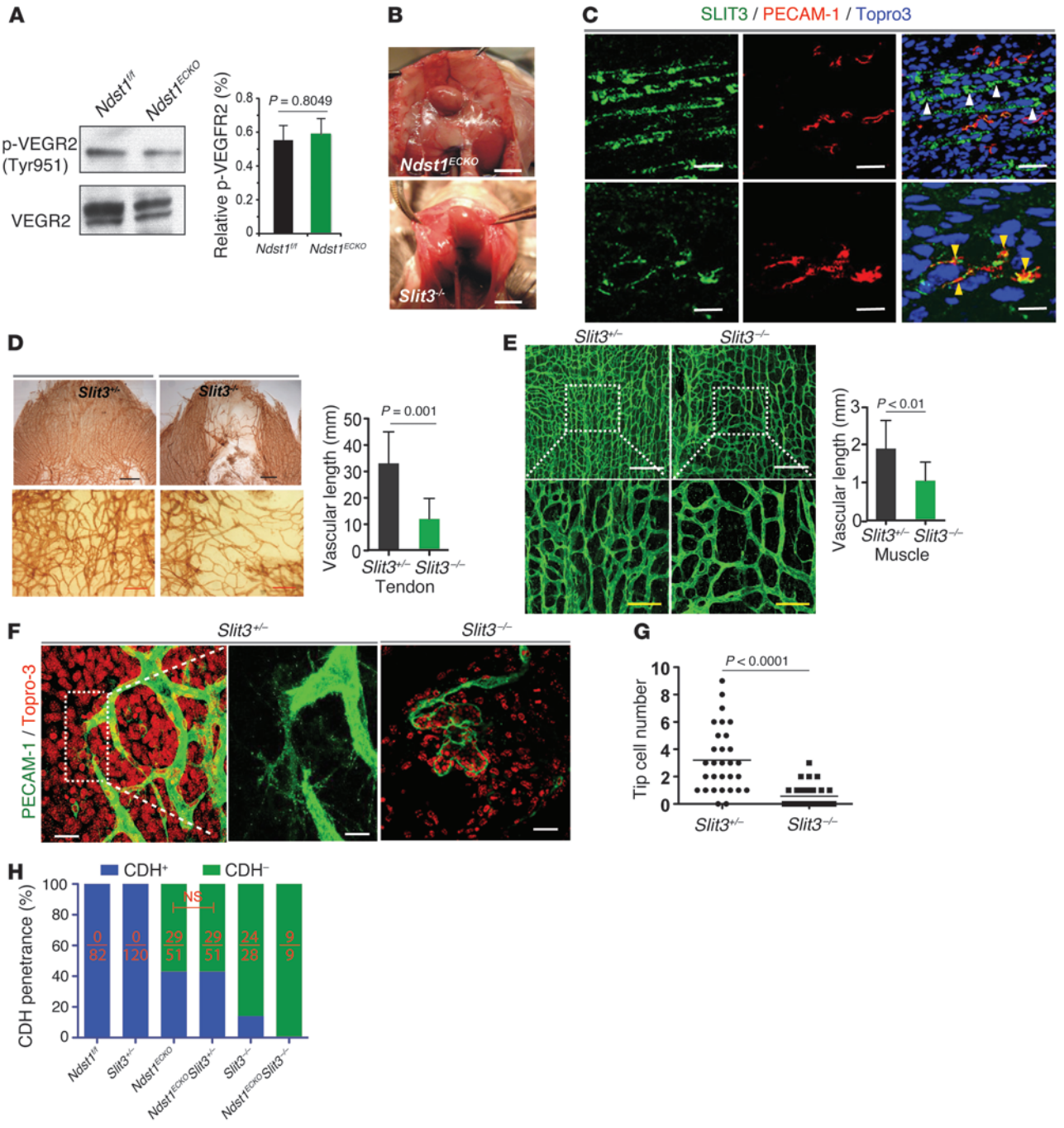

Figure 4

VEGF signaling in diaphragm, and *Ndst1*^{ECKO} mice phenocopy the developmental defects of *Slit3*$^{-/-}$ mice. (**A**) VEGFR2 phosphorylation (p-VEGFR2). Total VEGFR2 was immunoprecipitated with anti-VEGFR2 antibody from P1 diaphragms, then probed with anti-phosphotyrosine antibody by Western blot. No difference was observed between *Ndst1*$^{f/f}$ and *Ndst1*^{ECKO} diaphragms ($n = 3$). (**B**) *Ndst1*^{ECKO} and *Slit3*$^{-/-}$ mice showed similar central tendon CDH. (**C**) SLIT3 expression in diaphragm. E15.5 diaphragms were immunostained for SLIT3, PECAM-1, and Topro-3 (nuclei). SLIT3 was abundantly expressed by muscle cells (white arrowheads) and in vasculature (yellow arrowheads). (**D** and **E**) Disrupted developmental angiogenesis in *Slit3*$^{-/-}$ diaphragm. Whole-mount staining of E16.5 diaphragm with anti–PECAM-1 antibody showed that vascularization of the central tendon (**D**) and muscle (**E**) regions of *Slit3*$^{-/-}$, but not *Slit3*$^{+/-}$, diaphragm was disrupted, with reduced vascular density ($n = 4–6$). (**F** and **G**) Whole-mount staining of E16.5 diaphragms with anti–PECAM-1 antibody and Topro-3 to visualize tip cells. *Ndst1*^{ECKO} vasculature showed reduced tip cells and disrupted filopodia structure ($n = 4–6$). (**H**) Genetic interaction of endothelial *Ndst1* with *Slit3*. Introducing *Slit3*$^{+/-}$ did not alter CDH penetrance in *Ndst1*^{ECKO} mice. Number of CDH-positive animals relative to total animals examined is shown within each bar. Scale bars: 5 mm (**B**, top); 4 mm (**B**, bottom); 50 μm (**C**, top; and **E**, bottom); 0.5 mm (**D**, top); 0.2 mm (**D**, bottom); 200 μm (**E**, top); 20 μm (**C**, bottom; and **F**, left and right); 10 μm (**F**, middle).

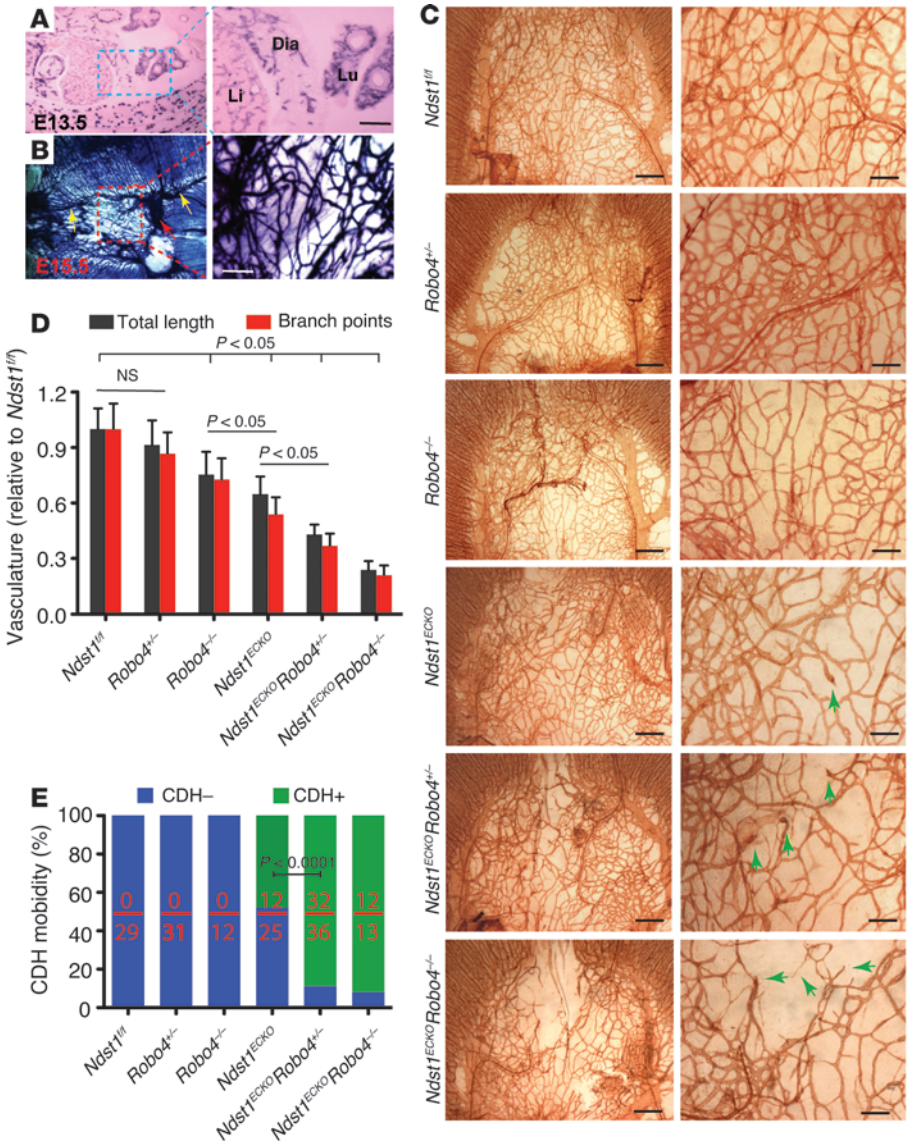

Figure 5

Compounding ROBO4 deficiency aggravates the angiogenic defect in *Ndst1*^{ECKO} mice and increases CDH penetrance. (**A** and **B**) ROBO4 expression in diaphragm vasculature. (**A**) Alkaline phosphatase (AP) expression in E13.5 embryo showed that ROBO4 was specifically expressed in blood vessels, including diaphragmatic vasculature. (**B**) AP expression in whole-mount E15.5 diaphragm. AP was expressed in diaphragmatic blood vessels, including the phrenic artery (yellow arrows), phrenic vein (red arrow), and capillary vessels (boxed region). (**C** and **D**) Genetic interaction of *Robo4* with endothelial *Ndst1*. (**C**) Vascularization in E16.5 *Robo4*$^{+/–}$ diaphragm was normal; however, introduction of *Robo4*$^{+/–}$ further reduced vascular density and increased misrouting of sprouting vessels (arrows) in *Ndst1*^{ECKO} diaphragm, exacerbating the vascular defects. (**D**) Vascular length and branch points were significantly reduced in *Ndst1*^{ECKO}*Robo4*$^{+/–}$ versus *Ndst1*^{ECKO} diaphragms (n = 3–5). (**E**) Genetic interaction of *Robo4* with endothelial *Ndst1* in CDH. CDH did not occur in *Robo4*$^{+/–}$ and *Robo4*$^{–/–}$ mice; however, introducing the *Robo4* mutations significantly increased CDH penetrance in *Ndst1*^{ECKO} mice. Number of CDH-positive animals relative to total animals examined is shown within each bar. Scale bars: 50 μm (**A**); 0.2 mm (**B** and **C**, right); 0.5 mm (**C**, left).

and the extracellular domain of ROBO4. SLIT3-N contains the first 2 leucine-rich repeat domains that correspond to the identified HS-binding site in SLIT2. Surface plasmon resonance (SPR) spectroscopy analysis showed that SLIT3-N bound heparin with high affinity and HS with moderate affinity (Figure 6, F and G). Moreover, fully desulfated heparin (Des-Hep), *N*-desulfated heparin (N-Des-Hep), and 6-*O*–desulfated heparin (6-Des-Hep) lost their ability to compete with heparin for SLIT3 binding, whereas 2-*O*–desulfated heparin (2-Des-Hep) did not (Figure 6G). Similar binding characteristics have been observed for SLIT3-C (27). These binding measurements were consistent with the effect of *Ndst1* deficiency on SLIT-ROBO signaling, reducing both *N*- and 6-*O*–sulfation of HS (Figure 6, B–D). In contrast to SLIT3, ROBO4 did not bind to HS in SPR analysis or in heparin affinity chromatography (data not shown). Collectively, these findings illustrated that EC HS interacts with SLIT3, but not ROBO4, to modulate SLIT3-ROBO4 signaling. Our results suggest a model whereby HS either presents SLIT3 to ROBO4 or induces changes in SLIT3 structure to facilitate ROBO4 interaction (Figure 6H), analogous to the well-accepted coreception function of HS in FGF-FGFR signaling (28).

Discussion

Numerous gene mutations, deletions, and duplications have been associated with CDH, based on genetic linkage in humans and examination of transgenic mouse models (3, 4). In the present study, we provided genetic evidence that deficiency of endothelial *Ndst1* also led to CDH in mice. This observation reveals *NDST1* as a new CDH-associated gene and also suggests the possibility that natural variation in HS composition might contribute to the incidence and severity of CDH. Loss-of-function mutations of *GPC3*, a cell surface HS proteoglycan, cause Simpson-Golabi-Behmel syndrome (21, 29). These patients display overgrowth of several tissues and exhibit the clinical spectrum of CDH. Our observations suggest that loss of the HS moiety of GPC3 may contribute to CDH occurrence in these patients. Thus, *NDST1* and other genes involved in HS biosynthesis and proteoglycans should be considered potential

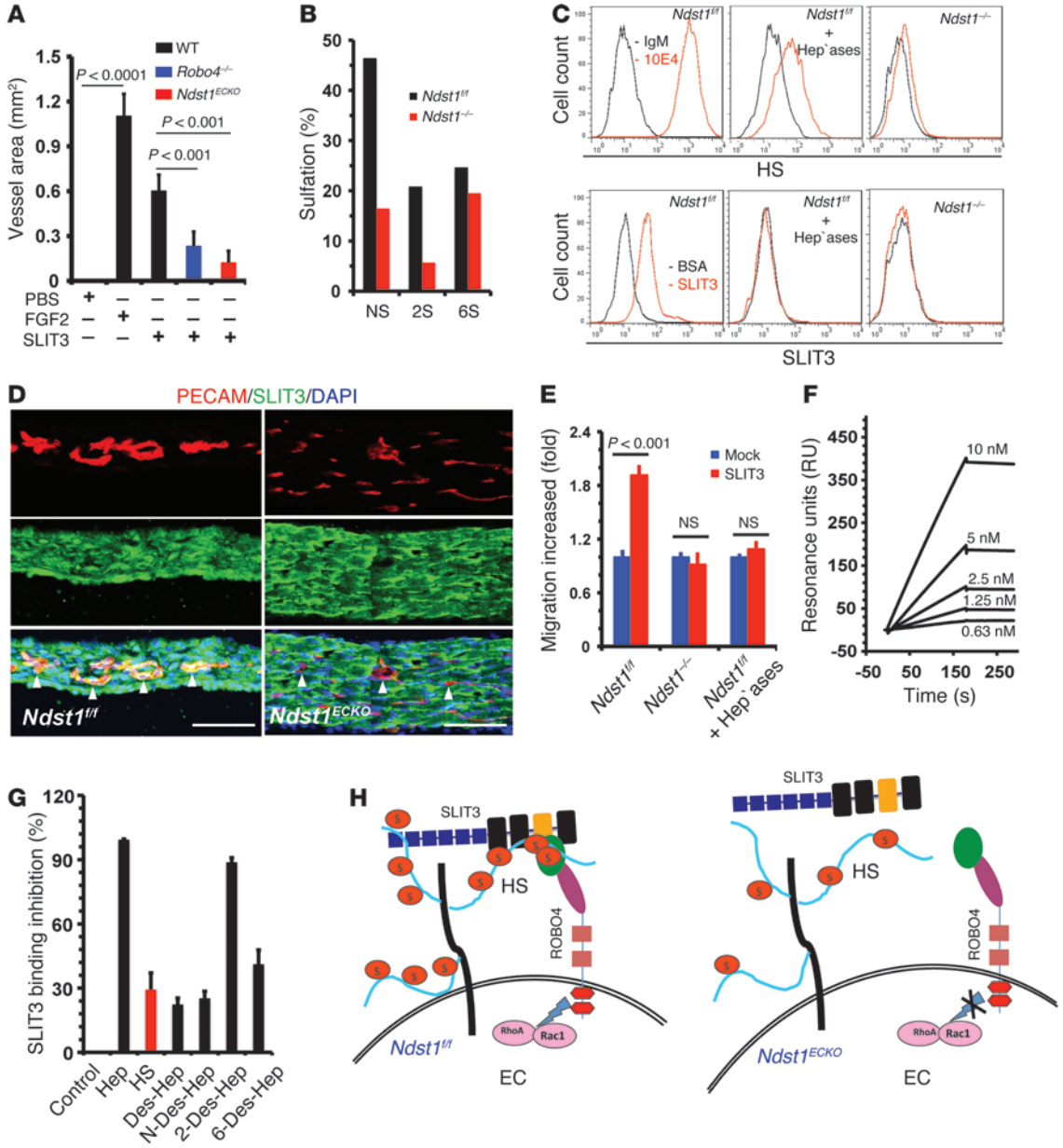

Figure 6

HS facilitates angiogenic SLIT3-ROBO4 signaling. (**A**) Mouse corneal micropocket angiogenesis assay showed disrupted SLIT3-induced angiogenesis in *Robo4*$^{-/-}$ and *Ndst1*^{ECKO} mice (n = 5–7). The PBS control showed no difference among the various genotypes and was pooled. (**B**) Disaccharide analysis showing that *Ndst1* deletion reduced *N*- and 2-*O*–sulfation by 60% and 6-*O*–sulfation by 20%. (**C**) SLIT3 binding to EC surface was *N*-sulfation dependent. Diaphragmatic ECs were stained with anti-HS antibody 10E4 or SLIT3 with background controls. Heparinase I–III treatment and *Ndst1* ablation both diminished cell surface SLIT3 binding. (**D**) SLIT3 binding to ECs (arrowheads) was diminished in *Ndst1*^{ECKO} diaphragm. Cryosection of P0 diaphragm was costained with biotinlyated SLIT3 and anti–PECAM-1 antibody. (**E**) SLIT3-induced EC migration in transwell analysis. Heparinase treatment and *Ndst1* ablation abolished SLIT3-induced EC migration (n = 3). (**F**) SLIT3 binding to heparin in SPR assay. SLIT3 showed dose-dependent binding to immobilized heparin (n = 3). (**G**) HS and heparin (Hep) competitively inhibited SLIT3 binding to immobilized heparin, and the inhibition was mainly *N*- and 6-*O*–sulfation dependent (n = 3). (**H**) Coreceptor model. HS binds SLIT3 on wild-type ECs to form the HS-SLIT3-ROBO4 ternary complexes that facilitate SLIT3-ROBO4 signaling. *Ndst1*$^{-/-}$ endothelial HS fails to bind SLIT3, resulting in disruption of HS-SLIT3-ROBO4 complex formation and subsequent angiogenic signaling. Scale bars: 40 μm (**D**).

candidates to explain CDH of unknown etiology or as modifiers that contribute to the severity of CDH in humans.

Developmental abnormalities of diaphragmatic muscle and tendon have been demonstrated to be attributable to CDH (4, 5). Our present data indicated that a vascular developmental defect may be the leading cause of the diaphragmatic muscle and tendon hypoplasia underlying the CDH phenotype in *Ndst1*^{ECKO} mice, suggesting that angiogenic defects may represent a new etiological mechanism of CDH in humans. Consistent with this idea, several CDH-associated genes, including those encoding FGFR, PDGFR,

HGF, MMPs, ROBO1, Fog2 and GATA4, are proangiogenic factors (3, 4). Thus, many of these models should be reevaluated to determine whether vascular development is impaired, thereby contributing to CDH occurrence.

We found that in *Ndst1*^{ECKO} mice, vascular development was uniquely disturbed in diaphragm, but not in other organs (such as lung), explaining the subsequent developmental abnormalities of muscle and tendon presented in diaphragm alone, not in the lung or other organs. Furthermore, recent studies have recognized that blood flow critically modulates vessel remodeling during development (30). It is possible that the abnormal diaphragmatic muscle and tendon development may alter the local blood supply, thereby compromising diaphragmatic vessel remodeling via a positive feedback mechanism to aggravate the vascular development defect in *Ndst1*^{ECKO} mice. We have not tested this idea due to technical challenges in our in vivo study.

Our molecular mechanism studies delineated that endothelial *Ndst1* ablation disrupted SLIT3-ROBO4 signaling–mediated EC function, leading to the diaphragmatic vascular development defect and subsequent CDH phenotype. We observed high SLIT3 expression in both ECs and diaphragmatic muscle cells. Moreover, SLIT3 bound strongly to diaphragmatic muscle cells, and myoblast cells expressed SLIT3 and ROBO1–ROBO2 during differentiation (Supplemental Figure 5, A and B), which suggests that SLIT3 may function via autocrine and paracrine mechanisms to modulate diaphragmatic muscle cell differentiation and function. We also observed downregulated SLIT3 expression in primary *Ndst1*^{ECKO} ECs (Supplemental Figure 5D), which suggests that the downregulation of SLIT3 expression might attenuate paracrine mechanism–mediated SLIT3 function on diaphragmatic muscle cells, thus contributing to the dysgenesis of *Ndst1*^{ECKO} diaphragm. Furthermore, the EC–extracellular matrix interaction is also essential for vascular development (12). In *Ndst1*^{ECKO} diaphragm vessels, collagen deposition and alignment were disturbed, suggesting that an EC-substrate interaction defect may also exist and contribute to the abnormal diaphragmatic vascular development in *Ndst1*^{ECKO} mice. All these potential mechanisms need to be further tested.

Our molecular mechanism studies initially examined whether *Ndst1* ablation attenuated VEGF signaling, leading to the vascular development defect in *Ndst1*^{ECKO} mice. We observed that NDST1 loss did not alter VEGFR2 activation in the developing *Ndst1*^{ECKO} diaphragm, and there was no synergistic effect between *VEGFR2*$^{+/-}$ and *Ndst1*^{ECKO} in diaphragmatic vascular development and in CDH. These observations are in agreement with prior reports, including that mice that lack the HS-binding isoforms of VEGF and *VEGFR2*$^{+/-}$ mice both do not develop CDH (15, 31). We therefore concluded that the localized angiogenesis defect in *Ndst1*^{ECKO} mice was not caused by a disruption of VEGF/VEGFR2 signaling.

As mentioned above, *FGFR* is also a CDH-associated gene and essentially requires HS for proper signaling (28). We previously observed that FGF2 binding to ECs and the subendothelial matrix was attenuated in *Ndst1*^{ECKO} mice (8), raising another possibility that *Ndst1* ablation might disturb FGF signaling, thus leading to the vascular development defect in *Ndst1*^{ECKO} diaphragm. We have not yet examined this issue, but a previous study investigated EC-specific FGFR1/FGFR2 double-knockout mice and did not report a CDH phenotype (32), which suggests that the FGF signaling defect in ECs might not be the molecular mechanism underlying the vascular and CDH phenotype in *Ndst1*^{ECKO} mice. In *Ndst1*^{ECKO} mice, *Ndst1* was also ablated in hematopoietic cells (8). *Ndst1* ablation did not alter the number of bone marrow cells and their subpopulations, nor did it alter hematopoietic cell trafficking under unchallenged conditions (8, 9), which suggests that it is also unlikely that *Ndst1* deficiency in hematopoietic cells contributes to the vascular development defect in *Ndst1*^{ECKO} diaphragm.

ROBO4 signaling has been demonstrated to possess both pro- and antiangiogenesis functions in vivo. For example, ROBO4 promotes intersomitic vessel development in zebrafish (19), and soluble ROBO4 inhibits angiogenesis in mice (33). Whereas in breast, ROBO4 counteracts VEGF signaling to inhibit angiogenesis and to stabilize the vasculature in skin and retina (18, 34, 35), in our current study, ROBO4 exhibited a proangiogenic function in diaphragm. The literature suggests that the pro- or antiangiogenic function of ROBO4 is ligand dependent. SLIT3-ROBO4 signaling was previously shown to promote angiogenesis (16), whereas SLIT2/UNC5B-ROBO4 interaction inhibits angiogenesis (18, 34, 35). Meanwhile, the ROBO expression profile may also regulate ROBO4 signaling. For example, ROBO1 — which is coexpressed with ROBO4 on ECs — binds SLIT2 and SLIT3, and may thereby compete with ROBO4 for the same ligand binding (16, 36). *Slit* and *Robo* gene expression appears to differ in breast, skin, retina, and diaphragm (16, 18, 34, 37), which may help explain the tissue-dependent functions of ROBO4 signaling in angiogenesis in these organs. Our present findings also showed an important essential function for HS in vascular development in the diaphragm and tied its activity to SLIT3-ROBO4 signaling. Interestingly, vascularization of other tissues appeared to be unaffected in *Ndst1*^{ECKO} mice, which suggests that developmental angiogenesis in the diaphragm appears to be exquisitely sensitive to HS composition. Further studies are needed to understand whether differences in HS content and composition contribute to the opposing effects of SLIT3-ROBO4 signaling in different tissues.

Methods

Animals. *Ndst1*^{ECKO} mice were generated by breeding *Ndst1*$^{f/f}$ mice with transgenic *Tie2Cre* mice (8, 9). *Tie2Cre* mice were bred with *Rosa26LacZ* reporter mice (38) to determine the specificity and efficacy of *Tie2Cre*-mediated *Ndst1* ablation in diaphragmatic endothelium. *Slit3*$^{-/-}$ mice were provided by D.M. Ornitz (Washington University School of Medicine, St. Louis, Missouri, USA; ref. 37), and *Robo4*$^{-/-}$ mice were generated as reported previously (18). All experimental mice were fully backcrossed to the C57BL/6 background and housed in barrier conditions under AAALAC-approved protocols.

Whole-mount staining of embryonic diaphragm. Whole-mount immunohistochemical staining of the embryonic diaphragm was performed as described previously (16). Briefly, embryonic diaphragms were dissected out, fixed in 4% PFA overnight, dehydrated in 100% methanol, and stored at –20°C until use. For HRP staining, endogenous peroxidase was quenched with 5% hydrogen peroxide in methanol before rehydration. After incubation with blocking buffer (2% nonfat milk plus 5% goat serum in PBS containing 0.2% Triton X-100 [PBX]), the diaphragm was incubated with anti–PECAM-1 antibody (MEC13.3, 1:200; BD Biosciences — Pharmingen) in PBX overnight at RT. Samples were washed with PBS 5 times and incubated overnight with biotinylated goat anti-rat antibody (1:50; BD Biosciences — Pharmingen) in PBX. After washing, the diaphragm was incubated with HRP-conjugated streptavidin for 2 hours prior to color development in DAB substrate (Vector Labs). Images were obtained under an Olympus CX41 microscope.

For whole-mount immunofluorescence staining, diaphragms were blocked and permeabilized with 10% normal goat serum in PBS containing

0.4% Triton X-100 for 2 hours, then incubated with primary antibodies in PBX containing 10% goat serum overnight at 4°C. Diaphragms were washed 5 times with PBX, incubated for 2 hours at RT with fluorescence-conjugated secondary antibody, and mounted with Vector Shield aqueous mounting medium. Primary antibodies used were anti–PECAM-1, rabbit anti-NG2 chondroitin sulfate proteoglycan (1:400; Millipore), anti-neurofilament (1:500; Chemicon), anti–myomesin B4 (1:800; Developmental Studies Hybridoma Bank), anti–α-SMA (clone 1A4, 1:400; Sigma-Aldrich), anti-desmin (1:400; DAKO), anti-GFP (1:400; Life Technologies), anti–α-actinin (clone EA53, 1:800; Sigma-Aldrich), and anti–caspase-3 (1:400; Millipore). Secondary antibodies included Alexa Fluor 488–conjugated goat anti-rat (1:100; Molecular Probes), Cy3-conjugated goat anti-rat (1:200; Molecular Probes), Texas red–conjugated goat anti-mouse (1:200; Molecular Probes), Alexa Fluor 488–conjugated goat anti-mouse (1:200; Molecular Probes), and Alexa Fluor 488–conjugated goat anti-rabbit (1:200; Molecular Probes). In some experiments, the diaphragm was counterstained with Topro-3 (1:1,000; Molecular Probes) or rhodamine-conjugated α-bungarotoxin (α-Bgt, 1:1,000; Invitrogen). Fluorescent images were obtained using a Zeiss LSM510 Meta confocal microscope and processed and quantified using LSM Image Browser and Image J software.

Microfill gel injection. Microfill gel injection was performed as described previously (39). In brief, mice were sacrificed and infused at physiological pressures with a curable yellow latex injection compound, Microfill MV-122 (Flowtech). After curing, mouse tissues were dissected and cleared in glycerol. The vascular architecture was visualized and documented using a dissecting microscope.

Immnuofluorescence staining of tissue sections. Immunofluorescence staining was performed as described previously (16). To detect SLIT3 and HS expression in the diaphragm, cryosections were fixed in precooled methanol and blocked in 1% BSA in PBS containing 5% goat serum followed by overnight incubation at 4°C with the following primary antibodies: rabbit anti-SLIT3 (1:200; Chemicon), anti-HS (10E4; Seikagaku), anti–β-gal (1:1,000; MP Biochemicals), anti–PECAM-1 (1:200). Samples were washed 3 times (5 minutes each) in PBS containing 0.05% Tween-20, incubated with secondary antibody for 1 hour at RT, and counterstained with Topro-3 (1:1,000) for 5 minutes before mounting. Secondary antibodies were Alexa Fluor 488–conjugated goat anti-mouse IgG, Alexa Fluor 488–conjugated goat anti-rabbit IgG, and Cy3-conjugated goat anti-rat IgG (all 1:200; Molecular Probes). Confocal imaging was captured using a Zeiss LSM510 Meta microscope. For in situ SLIT3 binding, tissue cryosections were incubated with biotinylated SLIT3 in PBS with 0.2% BSA for 1 hour at RT, followed by fixation in 4% PFA for 20 minutes, and then visualized by staining with FITC-conjugated streptavidin (1:2,000; Life Technologies). Diaphragm muscle fiber was revealed by staining with anti–α-actinin antibody. To label motor axons and postsynaptic acetylcholine receptor clusters, diaphragms were processed and stained as previously described (40).

BrdU labeling. BrdU labeling was achieved by intraperitoneal injection of pregnant mice with 50 mg/kg BrdU (MP Biochemicals) 2 hours prior to embryo harvest. For BrdU/EC whole-mount double staining, diaphragms were first fluorescently stained with anti–PECAM-1 antibody as described above and fixed again in 4% PFA for 30 minutes. DNA in the sample was then denatured with 2N HCL for 1 hour at RT and washed with PBS 3 times. Anti-BrdU antibody (clone G3G4, 1:400; Developmental Studies Hybridoma Bank) was applied and incubated overnight at RT, followed by incubation with Texas red–conjugated goat anti-mouse IgG antibody (1:200; Molecular Probes) for 4 hours at RT. For BrdU staining on the paraffin-embedded diaphragm, sections were denatured with 2 M hydrochloric acid for 30 minutes at 37°C, incubated with G3G4 (1:1,000) overnight at 4°C, and detected with a RTU VECTASTAIN universal ABC kit (Vector Labs) according to the manufacturer's instructions.

Detection of X-gal staining and AP activity. The diaphragm was isolated, fixed in 2% PFA and 0.2% glutaraldehyde in PBS, and then stained with X-gal solution overnight at 37°C. AP activity in *Robo4*$^{+/-}$ mice was detected as previously described (18). Briefly, diaphragms were fixed with 4% PFA and then heated in a 65°C water bath for 2 hours to inactivate endogenous AP, and color was developed with BM purple substrate (Roche) overnight. Samples were mounted in 80% glycerol after postfixing in 4% PFA and imaged using an Olympus CX41 microscope.

Hypoxia staining. Hypoxyprobe-1 (60 mg/kg; NPI Inc.) was injected into the peritoneum of pregnant mice. At 90 minutes after injection, embryos were harvested and dissected, then fixed in 4% PFA overnight. Detection of Hyproxyprobe-1 adducts in the diaphragm was performed by whole-mount staining with Hyproxyprobe-1–specific antibody (MAb1, 1:100; NPI Inc.) and secondary Alexa Fluor 488–conjugated goat anti-mouse IgG antibody (1:200).

Collagen staining. Staining of collagen fibers in diaphragmatic tendons were performed with Masson Trichrome staining kit (Richard-Allan Scientific) according to the manufacturer's instructions, except that staining with Weigert's iron hematoxylin was omitted.

Mouse primary EC isolation and immortalization. Primary mouse diaphragm *Ndst1*$^{f/f}$ ECs were isolated and immortalized as described previously (8). In brief, mouse diaphragm was minced and digested with collagenase (0.2%, w/v) at 37°C for 90 minutes. After filtration through a 40-μm mesh screen, crude cell preparations (3×10^7 cells/ml) were incubated with rat anti-mouse PECAM-1 antibody (MEC13.3) at 0.2 μg/10^6 cells for 15 minutes. After washing, cells were incubated with anti-rat IgG–coated beads (20 μl/10^7 cells; Dynal) for 15 minutes, then separated by flowing through a magnetic column. Cells that remained in the magnetic column were recovered and cultured in gelatin-coated culture plates with DMEM containing 20% FCS, 100 μg/ml heparin, 100 μg/ml EC growth supplement, nonessential amino acids, sodium pyruvate, L-glutamine, and antibiotics. Primary ECs showed a cobblestone-like morphology in culture, remained >98% pure at passage 1 (as assessed by both anti–PECAM-1 and anti–von Willebrand factor antibody staining), and responded vigorously to VEGF-induced cell migration, demonstrating their homogeneity and proper function. A fraction of the primary ECs was immortalized with simian virus 40 large T antigen and subcloned in order to obtain a *Ndst1*$^{f/f}$ mother EC line. The daughter *Ndst1*$^{-/-}$ line was generated by infecting *Ndst1*$^{f/f}$ cells with the adeno-Cre virus, followed by single-cell cloning.

Recombinant SLIT3 proteins. Recombinant human SLIT3 N-terminal fragment (aa 34–919) was purchased from R&D Systems or was expressed in house. The N-terminal fragment was cloned into a modified pcDNA 3.1 vector (Invitrogen) with an HPC4 tag at the N terminus and a 6x-His tag at the C terminus (27). The construct was transfected into mouse neuroblastoma N2A cells (ATCC), and stably expressing clones were obtained. Control stable clones expressed the empty vector. Conditioned media (CM) was collected after culturing the stably expressing cells in serum-free medium for 60–72 hours and used for functional studies without further purification.

Corneal micropocket angiogenesis assay. Corneal micropocket angiogenesis assay was performed as described previously (16). In brief, slow-releasing pellets were prepared by homogeneously mixing test factors with sucralfate and 12% hydron (both Sigma-Aldrich). 6- to 8-week-old experimental mice were anesthetized with Avertin (400 mg/kg; Sigma-Aldrich) prior to implantation of pellets into the cornea. Animals were placed in lateral recumbency, and the globe was carefully exposed by retracting the eyelids with forceps.

A von Graefe knife no. 3 was used to create a 0.3- to 0.4-mm linear, midstromal incision in the center of the cornea. A micropocket was then created from the incision toward the lateral limbus with sliding motions

of the microknife and with care not to perforate the cornea. A pellet containing BSA, FGF2, or SLIT3 was implanted into the micropocket, and topical erythromycin ointment was applied. After 5 days, corneas were examined with slit lamp biomicroscopy (SL14; Kowa) and photographed under a dissection microscope (Nikon). Neovascularization in mouse corneas was quantified using Image J software as follows: 0.063 × vessel length (in mm) × clock hour.

Cell motility. Cell migration was assessed by Boyden chamber transwell migration (16, 41). Briefly, serum-starved ECs were loaded into transwell inserts with 8-μm pores (Costar), and the SLIT3 or CM prepared from SLIT3-expressing N2A cells was added to the lower chamber. After 16 hours, cells on the top side of the membrane were wiped off, and cells on the bottom side were fixed, stained with 0.09% crystal violet, and visualized under a dissection microscope. The total number of cells in 5 random fields was counted, and results were expressed as fold increase over background (measured in the presence of BSA or control CM).

Interaction of heparinoids with SLIT3 in SPR analysis. Heparinoids used were porcine intestinal heparin (Hep; 16 kDa), porcine intestinal HS (Celsus Laboratories), and chondroitin sulfate A (20 kDa) from porcine rib cartilage (Sigma-Aldrich). Des-Hep (14 kDa), N-Des-Hep (14 kDa), 2-Des-Hep (13 kDa), and 6-Des-Hep (13 kDa) were prepared as described in our previous studies (Supplemental Figure 4F and refs. 23, 41–43). SPR measurements were performed with biotinylated heparin immobilized on streptavidin-coated Sensor SA chips on a BIAcore 3000 using BIA evaluation software (version 4.0.1) (23, 27, 41). For direct binding analysis, SLIT3 protein samples were diluted in buffer containing 0.01 M HEPES, 0.15 M NaCl, 3 mM EDTA, and 0.005% surfactant P20, at pH 7.4. Different dilutions of the protein samples were injected at a flow rate of 30 μl/min. At the end of the sample injection, buffer was flowed over the sensor surface to allow dissociation. After 3 minutes, the sensor surface was regenerated by injecting 30 μl of 2 M NaCl. The response was monitored as a function of time (sensorgram) at 25°C. For competition studies, 10 nM SLIT3 protein was premixed with 1,000 nM test glycosaminoglycan and injected over the heparin chip at a flow rate of 30 μl/min. After each run, a dissociation period and regeneration protocol was performed as described above. For each set of competition experiments, a control experiment with protein without glycosaminoglycan was performed to ensure the surface was completely regenerated and that the results obtained between runs were comparable.

Rho GTPase activity analysis. Rac1, RhoA, and Cdc42 activation induced by SLIT3 was assessed, following the protocols described in the EZ-Detect Rho GTPase assay Kit (Pierce) (16). Briefly, serum-starved ECs were treated for 0–30 minutes with SLIT3-containing CM and then lysed. Lysates were incubated for 60 minutes with a GST fusion protein that was preconjugated to glutathione-sepharose beads and contained the CRIB domain of p21 activated kinase (PAK1), followed by 3 washes with Rho lysis buffer. The GTP-bound forms of Rac1 or Cdc42 associated with GST-CRIB were quantified by Western blot analysis using a monoclonal antibody against Rac1 or Cdc42. For Rho pulldown assays, GST-rhotekin-RBD beads were used, and the GST-rhotekin-RBD–bound RhoA was similarly quantified using a monoclonal antibody against RhoA.

Statistics. Data are presented as mean ± SEM. Statistical significance was determined by 2-tailed Student's *t* test or multigroup ANOVA and by χ^2 test for comparison of CDH penetrance. A *P* value less than 0.05 was considered statistically significant. Power analysis determined sample size estimation.

Study approval. The Institutional Animal Care and Use Committee of the University of Georgia approved animal studies.

Acknowledgments

This work was supported by NIH grants R01HL093339 (to L. Wang), RR005351/GM103390 (to L. Wang), HL62244 and GM38060 (to F. Zhang and R.J. Linhardt), and P01 HL107150 (to J.D. Esko) and by the Canadian Institute for Health Research (to J.J. Greer). We thank David M. Ornitz for providing the *Slit3*$^{-/-}$ mice and Karen Howard for her English revision of the manuscript.

Received for publication May 16, 2013, and accepted in revised form October 11, 2013.

Address correspondence to: Lianchun Wang, Complex Carbohydrate Research Center, University of Georgia, 315 Riverbend Road, Athens, Georgia 30602-4712, USA. Phone: 706.542.6445; Fax: 706.542.4412; E-mail: Lwang@ccrc.uga.edu. Or to: Jeffrey D. Esko, Department of Cellular and Molecular Medicine, Glycobiology Research and Training Center, University of California at San Diego, La Jolla, California 92093-0687, USA. Phone: 858.822.1100; Fax: 858.534.5611; E-mail: jesko@ucsd.edu.

1. Nobuhara KK, Lund DP, Mitchell J, Kharasch V, Wilson JM. Long-term outlook for survivors of congenital diaphragmatic hernia. *Clin Perinatol*. 1996;23(4):873–887.
2. Veenma DC, de Klein A, Tibboel D. Developmental and genetic aspects of congenital diaphragmatic hernia. *Pediatr Pulmonol*. 2012;47(6):534–545.
3. Brady PD, Srisupundit K, Devriendt K, Fryns JP, Deprest JA, Vermeesch JR. Recent developments in the genetic factors underlying congenital diaphragmatic hernia. *Fetal Diagn Ther*. 2010;29(1):25–39.
4. Bielinska M, et al. Molecular genetics of congenital diaphragmatic defects. *Ann Med*. 2007; 39(4):261–274.
5. Clugston RD, Greer JJ. Diaphragm development and congenital diaphragmatic hernia. *Semin Pediatr Surg*. 2007;16(2):94–100.
6. Sarrazin S, Lamanna WC, Esko JD. Heparan sulfate proteoglycans. *Cold Spring Harb Perspect Biol*. 2011;3(7):pii: a004952.
7. Pilia G, et al. Mutations in GPC3, a glypican gene, cause the Simpson-Golabi-Behmel overgrowth syndrome. *Nat Genet*. 1996;12(3):241–247.
8. Wang L, Fuster M, Sriramarao P, Esko JD. Endothelial heparan sulfate deficiency impairs L-selectin- and chemokine-mediated neutrophil trafficking during inflammatory responses. *Nat Immunol*. 2005;6(9):902–910.
9. Fuster MM, et al. Genetic alteration of endothelial heparan sulfate selectively inhibits tumor angiogenesis. *J Cell Biol*. 2007;177(3):539–549.
10. Kisanuki YY, Hammer RE, Miyazaki J, Williams SC, Richardson JA, Yanagisawa M. Tie2-Cre transgenic mice: a new model for endothelial cell-lineage analysis in vivo. *Dev Biol*. 2001;230(2):230–242.
11. Abramsson A, et al. Defective N-sulfation of heparan sulfate proteoglycans limits PDGF-BB binding and pericyte recruitment in vascular development. *Genes Dev*. 2007;21(3):316–331.
12. Stenzel D, Nye E, Nisancioglu M, Adams RH, Yamaguchi Y, Gerhardt H. Peripheral mural cell recruitment requires cell-autonomous heparan sulfate. *Blood*. 2009;114(4):915–924.
13. Song JQ, Teng X, Cai Y, Tang CS, Qi YF. Activation of Akt/GSK-3beta signaling pathway is involved in intermedin(1-53) protection against myocardial apoptosis induced by ischemia/reperfusion. *Apoptosis*. 2009;14(11):1299–1307.
14. Fuster MM, Wang L. Endothelial heparan sulfate in angiogenesis. *Prog Mol Biol Transl Sci*. 2010; 93:179–212.
15. Shalaby F, et al. Failure of blood-island formation and vasculogenesis in Flk-1-deficient mice. *Nature*. 1995;376(6535):62–66.
16. Zhang B, Dietrich UM, Geng JG, Bicknell R, Esko JD, Wang L. Repulsive axon guidance molecule Slit3 is a novel angiogenic factor. *Blood*. 2009; 114(19):4300–4309.
17. Park KW, et al. Robo4 is a vascular-specific receptor that inhibits endothelial migration. *Dev Biol*. 2003; 261(1):251–267.
18. Jones CA, et al. Robo4 stabilizes the vascular network by inhibiting pathologic angiogenesis and endothelial hyperpermeability. *Nature medicine*. 2008;14(4):448–453.
19. Bedell VM, et al. roundabout4 is essential for angiogenesis in vivo. *Proc Natl Acad Sci U S A*. 2005; 102(18):6373–6378.
20. Huminiecki L, Gorn M, Suchting S, Poulsom R, Bicknell R. Magic roundabout is a new member of the roundabout receptor family that is endothelial specific and expressed at sites of active angiogenesis. *Genomics*. 2002;79(4):547–552.
21. Klaassens M, et al. Congenital diaphragmatic hernia associated with duplication of 11q23-qter. *Am J Med Genet A*. 2006;140(14):1580–1586.
22. Wijelath E, et al. Multiple mechanisms for exogenous heparin modulation of vascular endothelial growth factor activity. *J Cell Biochem*. 2010; 111(2):461–468.
23. Zhang F, Ronca F, Linhardt RJ, Margolis RU. Structural determinants of heparan sulfate interactions with Slit proteins. *Biochem Biophys Res Commun*. 2004;317(2):352–357.

24. Liang Y, et al. Mammalian homologues of the Drosophila slit protein are ligands of the heparan sulfate proteoglycan glypican-1 in brain. *J Biol Chem*. 1999; 274(25):17885–17892.
25. Fukuhara N, Howitt JA, Hussain SA, Hohenester E. Structural and functional analysis of slit and heparin binding to immunoglobulin-like domains 1 and 2 of Drosophila Robo. *J Biol Chem*. 2008; 283(23):16226–16234.
26. Hussain SA, et al. A molecular mechanism for the heparan sulfate dependence of slit-robo signaling. *J Biol Chem*. 2006;281(51):39693–39698.
27. Condac E, et al. The C-terminal fragment of axon guidance molecule Slit3 binds heparin and neutralizes heparin's anticoagulant activity. *Glycobiology*. 2012;22(9):1183–1192.
28. Yayon A, Klagsbrun M, Esko JD, Leder P, Ornitz DM. Cell surface, heparin-like molecules are required for binding of basic fibroblast growth factor to its high affinity receptor. *Cell*. 1991; 64(4):841–848.
29. DeBaun MR, Ess J, Saunders S. Simpson Golabi Behmel syndrome: progress toward understanding the molecular basis for overgrowth, malformation, and cancer predisposition. *Mol Genet Metab*. 2001; 72(4):279–286.
30. Eilken HM, Adams RH. Dynamics of endothelial cell behavior in sprouting angiogenesis. *Curr Opin Cell Biol*. 2010;22(5):617–625.
31. Carmeliet P, et al. Impaired myocardial angiogenesis and ischemic cardiomyopathy in mice lacking the vascular endothelial growth factor isoforms VEGF164 and VEGF188. *Nat Med*. 1999; 5(5):495–502.
32. Lavine KJ, et al. Fibroblast growth factor signals regulate a wave of Hedgehog activation that is essential for coronary vascular development. *Genes Dev*. 2006;20(12):1651–1666.
33. Suchting S, Heal P, Tahtis K, Stewart LM, Bicknell R. Soluble Robo4 receptor inhibits in vivo angiogenesis and endothelial cell migration. *FASEB J*. 2005; 19(1):121–123.
34. Marlow R, et al. Vascular Robo4 restricts proangiogenic VEGF signaling in breast. *Proc Natl Acad Sci U S A*. 2010;107(23):10520–10525.
35. Koch AW, et al. Robo4 maintains vessel integrity and inhibits angiogenesis by interacting with UNC5B. *Dev Cell*. 2011;20(1):33–46.
36. Carmeliet P, Tessier-Lavigne M. Common mechanisms of nerve and blood vessel wiring. *Nature*. 2005; 436(7048):193–200.
37. Yuan W, Rao Y, Babiuk RP, Greer JJ, Wu JY, Ornitz DM. A genetic model for a central (septum transversum) congenital diaphragmatic hernia in mice lacking Slit3. *Proc Natl Acad Sci U S A*. 2003; 100(9):5217–5222.
38. Soriano P. Generalized lacZ expression with the ROSA26 Cre reporter strain. *Nat Genet*. 1999; 21(1):70–71.
39. Grunstein J, Masbad JJ, Hickey R, Giordano F, Johnson RS. Isoforms of vascular endothelial growth factor act in a coordinate fashion To recruit and expand tumor vasculature. *Mol Cell Biol*. 2000; 20(19):7282–7291.
40. Jaworski A, Burden SJ. Neuromuscular synapse formation in mice lacking motor neuron- and skeletal muscle-derived Neuregulin-1. *J Neurosci*. 2006; 26(2):655–661.
41. Zhang S, et al. Heparin-induced leukocytosis requires 6-O-sulfation and is caused by blockade of selectin- and CXCL12 protein-mediated leukocyte trafficking in mice. *J Biol Chem*. 2012;287(8):5542–5553.
42. Wang L, Brown JR, Varki A, Esko JD. Heparin's anti-inflammatory effects require glucosamine 6-O-sulfation and are mediated by blockade of L- and P-selectins. *J Clin Invest*. 2002;110(1):127–136.
43. Zhang F, Moniz HA, Walcott B, Moremen KW, Linhardt RJ, Wang L. Characterization of the interaction between Robo1 and heparin and other glycosaminoglycans. *Biochimie*. 2013; pii:S0300-9084(13)00290-3.